

# MAXI J1820+070 with *NuSTAR* I. An increase in variability frequency but a stable reflection spectrum: coronal properties and implications for the inner disc in black hole binaries

D. J. K. Buisson,<sup>1★</sup> A. C. Fabian<sup>1</sup>, D. Barret,<sup>2,3</sup> F. Fürst,<sup>4</sup> P. Gandhi<sup>5</sup>, J. A. García,<sup>6,7</sup> E. Kara,<sup>8</sup> K. K. Madsen,<sup>6</sup> J. M. Miller,<sup>9</sup> M. L. Parker<sup>10</sup>, A. W. Shaw<sup>10</sup>, J. A. Tomsick<sup>11</sup> and D. J. Walton<sup>1</sup>

<sup>1</sup>*Institute of Astronomy, University of Cambridge, Madingley Road, CB3 0HA Cambridge, UK*

<sup>2</sup>*UPS-OMP; IRAP; Université de Toulouse; 9 Av. colonel Roche, BP 44346, F-31028 Toulouse cedex 4, France*

<sup>3</sup>*CNRS; Institut de Recherche en Astrophysique et Planétologie; 9 Av. colonel Roche, BP 44346, F-31028 Toulouse cedex 4, France*

<sup>4</sup>*European Space Astronomy Centre (ESA/ESAC), E-28691 Villanueva de la Cañada, Madrid, Spain*

<sup>5</sup>*Department of Physics and Astronomy, University of Southampton, Highfield, SO17 1BJ Southampton, UK*

<sup>6</sup>*Cahill Center for Astrophysics, 1216 E. California Blvd, California Institute of Technology, Pasadena, CA 91125, USA*

<sup>7</sup>*Dr. Karl Remeis-Observatory and Erlangen Centre for Astroparticle Physics, Sternwartstr 7, D-96049 Bamberg, Germany*

<sup>8</sup>*Department of Astronomy, University of Maryland, College Park, MD 20742-2421, USA*

<sup>9</sup>*Department of Astronomy, University of Michigan, 1085 South University Avenue, Ann Arbor, MI 48109-1104, USA*

<sup>10</sup>*Department of Physics, University of Alberta, CCIS 4-181, Edmonton, AB T6G 2E1, Canada*

<sup>11</sup>*Space Sciences Laboratory, 7 Gauss Way, University of California, Berkeley, CA 94720-7450, USA*

Accepted 2019 September 20. Received 2019 September 19; in original form 2019 May 31

## ABSTRACT

MAXI J1820+070 (optical counterpart ASASSN-18ey) is a black hole candidate discovered through its recent very bright outburst. The low extinction column and long duration at high flux allow detailed measurements of the accretion process to be made. In this work, we compare the evolution of X-ray spectral and timing properties through the initial hard state of the outburst. We show that the inner accretion disc, as measured by relativistic reflection, remains steady throughout this period of the outburst. Nevertheless, subtle spectral variability is observed, which is well explained by a change in coronal geometry. However, characteristic features of the temporal variability – low-frequency roll-over and quasi-periodic oscillation frequency – increase drastically in frequency, as the outburst proceeds. This suggests that the variability time-scales are governed by coronal conditions rather than solely by the inner disc radius. We also find a strong correlation between X-ray luminosity and coronal temperature. This can be explained by electron pair production with a changing effective radius and a non-thermal electron fraction of  $\sim 20$  per cent.

**Key words:** accretion, accretion discs – black hole physics – X-rays: binaries.

## 1 INTRODUCTION

The transfer of matter in accretion produces variability on all time-scales from the complete transfer of matter down to the shortest associated with the system. In black hole binaries (BHBs), accretion occurs on to a particularly compact object, so time-scales are correspondingly short and accretion episodes can evolve quickly (compared to, for example, active galactic nuclei, AGN). BHBs are therefore ideal laboratories for observations of long-time-scale accretion processes.

X-ray emission from BHBs occurs principally in two accretion states (along with some additional transitional states), commonly referred to as soft and hard (e.g. review by Remillard & McClintock 2006). In the soft state, emission is dominated by pseudo-blackbody thermal emission from the disc (Novikov & Thorne 1973; Shakura & Sunyaev 1973), which extends to the innermost stable circular orbit (ISCO, Gierliński & Done 2004; Steiner et al. 2010). Contrastingly, hard state emission is dominated by coronal emission produced by inverse-Compton scattering in a cloud of hot electrons (Thorne & Price 1975; Sunyaev & Truemper 1979), which has a spectrum approximated by a power law with a high-energy cut-off.

A complete understanding of the physical changes between these two states is not yet well known: In particular, the nature of the

\* E-mail: [djkb2@cam.ac.uk](mailto:djkb2@cam.ac.uk)

inner disc during the hard state is still not agreed upon. In some models, the disc is truncated and the accreting material forms a hot inner flow with high ionization, which produces the Comptonized spectrum (Esin, McClintock & Narayan 1997; Done, Gierliński & Kubota 2007; Gilfanov 2010). However, this is sometimes at odds with the inner radius measured spectrally, which is often small (Park et al. 2004; Reis et al. 2013; Parker et al. 2015). In this case, the central part of the disc is cool and dense enough to reflect but only emits a small fraction of the energy released by accretion thermally (Reis, Fabian & Miller 2010), as energy is extracted magnetically to power a corona positioned above the disc, possibly as the base of a jet (e.g. Markoff, Nowak & Wilms 2005; Fabian et al. 2012).

X-ray emission from BHBs also shows fast variability on many time-scales. Often, specific frequencies show stronger variability, known as quasi-periodic oscillations (QPOs; e.g. van der Klis 2006). These QPOs give characteristic time-scales to the system’s variability, so can be used to infer physical properties when combined with theoretical models for their production.

QPOs can be divided into various classes; the primary distinction being between high-frequency ( $\sim 10 - 10^3$  Hz) and low-frequency ( $\sim 10^{-2} - 10$  Hz) QPOs. Low-frequency QPOs are further divided into subtypes depending on their coherence and the strength of different harmonics (Wijnands, Homan & van der Klis 1999; Homan et al. 2001; Remillard et al. 2002). Unfortunately, there is not yet an accepted explanation for the production of any of the classes of QPOs. In the hot inner flow model, the boundary between the disc and the hot inner flow provides a possible source of QPOs. The inner flow can undergo Lense–Thirring precession, with frequencies similar to those seen in low-frequency QPOs (Stella, Vietri & Morsink 1999; Ingram, Done & Fragile 2009; Ingram & Done 2011).

New observations of bright sources with the new generation of telescopes have the potential to resolve these questions.

### 1.1 MAXI J1820+070

MAXI J1820+070 is a recently discovered transient source, which is likely to be a BHB system. The optical counterpart to MAXI J1820+070, ASASSN-18ey, was detected by the All-Sky Automated Search for Supernovae (Shappee et al. 2014) on 2018 March 3, several days before the announcement of the X-ray source (Kawamuro et al. 2018) and their association was proposed (Denisenko 2018) on 2018 March 11. The low extinction column and long outburst have allowed a wealth of data to be collected in many wavebands.

The X-ray outburst began with an initial fast rise (to MJD 58200) and slow decay (till around MJD 58290) across the full X-ray band; once the flux reached roughly one quarter of the peak, the source re-brightened substantially before the hard X-ray flux dropped dramatically (around MJD 58305) as the source transitioned into the soft state. After over 2 months in the soft state, the hard X-ray flux increased (from around MJD 58380) as the source re-entered the hard state before fading into quiescence. Fig. 1 shows the hard (15–50 keV) X-ray light curve from the *Neil Gehrels Swift Observatory* Burst Alert Telescope (*Swift*-BAT) transient monitor (Gehrels et al. 2004; Krimm et al. 2013). Fig. 2 shows a hardness–intensity diagram of the outburst from *Neutron star Interior Composition ExploreR* (*NICER*; Gendreau et al. 2016) data.

*International Gamma Ray Astrophysics Laboratory* (Winkler et al. 2003) observations show differences in the spectra between the rise and decay and a hard tail above the Compton cut-off, which

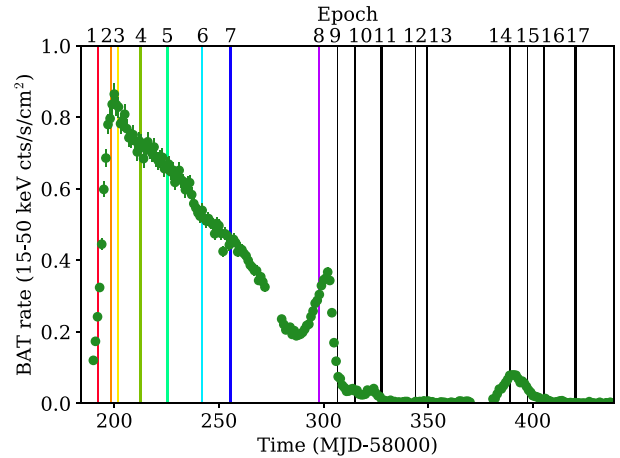


**Figure 1.** Light curve of MAXI J1820+070 from *Swift*-BAT (green) with times of *NuSTAR* observations shown as the vertical bars. Observations analysed here are in colour; later observations are in black.

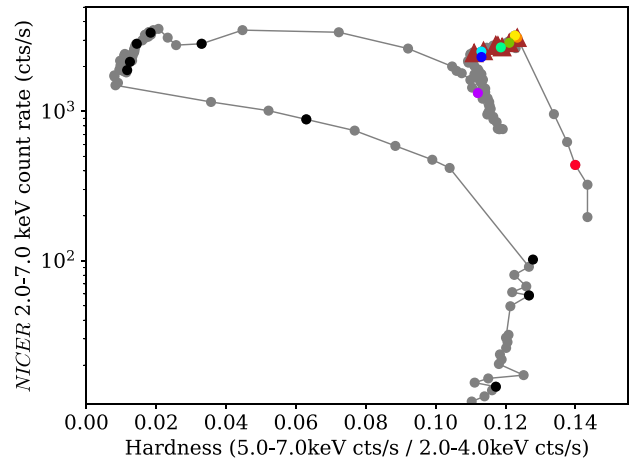


**Figure 2.** Hardness–intensity diagram of MAXI J1820+070 from *NICER* data (grey). The day coincident with each *NuSTAR* observation is shown in the colour matching Fig. 1. For comparison, the *NICER* observations analysed in Kara et al. (2019) are shown as the brown triangles.

may be from a jet (Roques & Jourdain 2019). Combining *Monitor of All-sky X-ray Image* (*MAXI*; Matsuoka et al. 2009) with *Swift*-BAT data shows a typical photon index of  $\Gamma \sim 1.5$  and an electron temperature of  $kT_e \sim 50$  keV (Shidatsu et al. 2018).

The start of the optical outburst preceded the X-ray by around 7 d; light curves and spectra show broad double-peaked emission lines and variability in the outburst and pre-outburst emission, typical of low-mass X-ray binaries (Tucker et al. 2018).

QPOs have been observed in the emission from MAXI J1820+070 in many wavebands, from optical (Fiori et al. 2018; Yu et al. 2018a,b; Zampieri et al. 2018) to hard X-ray (Mereminskiy et al. 2018). The frequency of these QPOs increases with time (Homan et al. 2018) during the first part of the outburst and, over the initial few *Nuclear Spectroscopic Telescope Array* (*NuSTAR*; Harrison et al. 2013) hard X-ray observations, this increase was suggested to be exponential with time (Buisson et al. 2018). Reverberation lags, differences in arrival time between direct coronal and reflected emission, have also been detected in the

**Table 1.** List of *NuSTAR* observations of MAXI J1820+070. The observation length is significantly longer than the effective exposure due to dead-time, orbital, and other gaps. Since pairs of observations are sometimes closely spaced, we divide the data sets into several epochs for analysis purposes. Only epochs before the transition to the soft state are considered here.

OBSID	Start time	Observation length ks <sup>-1</sup>	Count rate (incident cts s <sup>-1</sup> )	Live fraction	Epoch	State
90401309002	2018-03-14T20:26:09	43.0	157	0.62	1	Hard
90401309004	2018-03-21T00:31:09	14.2	664	0.28	2	Hard
90401309006	2018-03-21T07:06:09	31.7	679	0.28	2	Hard
90401309008	2018-03-24T12:31:09	20.7	701	0.27	3	Hard
90401309010	2018-03-24T20:26:09	14.9	703	0.27	3	Hard
90401309012	2018-04-04T04:31:09	84.4	624	0.29	4	Hard
90401309013	2018-04-16T22:21:09	8.4	602	0.3	5	Hard
90401309014	2018-04-17T06:31:09	55.5	609	0.3	5	Hard
90401309016	2018-05-03T18:51:09	60.5	512	0.34	6	Hard
90401309018	2018-05-17T03:36:09	13.1	407	0.37	7	Hard
90401309019	2018-05-17T14:26:09	43.9	440	0.37	7	Hard
90401309021	2018-06-28T03:56:09	77.7	265	0.5	8	Hard
90401309023	2018-07-07T08:36:09	38.1	461	0.33	9	Soft
90401309025	2018-07-15T17:51:09	43.7	321	0.39	10	Soft
90401309027	2018-07-28T01:11:09	83.3	237	0.45	11	Soft
90401309029	2018-08-13T14:26:09	26.5	158	0.54	12	Soft
90401309031	2018-08-19T07:26:09	58.7	131	0.58	13	Soft
90401309033	2018-09-27T21:51:09	67.0	108	0.68	14	Hard
90401309035	2018-10-06T07:11:09	38.1	46	0.81	15	Hard
90401309037	2018-10-13T22:46:09	82.4	12	0.9	16	Hard
90401309039	2018-10-29T01:11:09	96.1	3	0.93	17	Hard

X-ray variability; these lags shorten as the variability frequencies increase, suggesting that the corona becomes more compact (Kara et al. 2019).

The distance to MAXI J1820+070 is still moderately uncertain. Among the first set of X-ray binary distances to be derived directly from optical astrometry (rather than indirect photometric and spectroscopic methods), *Gaia* measurements of the system in quiescence give a parallax of  $0.31 \pm 0.11$  milliarcsec, which corresponds to a distance of  $3.5^{+2.2}_{-1.0}$  kpc (Gandhi et al. 2019). This should be improved in the next *Gaia* data release, especially considering the long interval over which the source remained bright.

*NuSTAR* is the first X-ray telescope to focus hard ( $\gtrsim 10$  keV) X-rays. It uses CdZnTe detectors with a triggered readout, allowing observations of bright sources to be free of pile-up, which degrades conventionally read CCDs. These capabilities have allowed *NuSTAR* to perform several observations of MAXI J1820+070; the times of these are shown in Fig. 1 as the coloured vertical bands (these colours are used to indicate the same epoch throughout this work), showing that *NuSTAR* observations occurred during all of these stages of the outburst.

The accumulated data set is vast and a full analysis is beyond the scope of a single work. Here, we focus on a comparison between the evolution of the spectral and timing properties during the initial hard state of the outburst. We summarize the data used in Section 2; present an overview of the outburst properties in Section 3.1 and describe details of power spectra in Section 3.2. We comment on possible interpretations of our findings in Section 4 and summarize in Section 5.

## 2 OBSERVATIONS AND DATA REDUCTION

We analyse data from all *NuSTAR* observations of MAXI J1820+070 before the transition to the soft state, as

shown in Table 1. For data transfer reasons, some pseudo-continuous observation periods were divided into separate OBSIDs; we reduce these sections separately but treat them as a single observation for later analysis. We refer to different observations as epochs, numbered as in Table 1.

The data were reduced with the *NuSTAR* Data Analysis Software (NUSTARDAS) pipeline, version 1.8.0 and CALDB version 20171002. When filtering for passages through the South Atlantic Anomaly, ‘saamode’ was set to ‘strict’ and ‘tentacle’ to ‘yes’. Following the recommendations of the *NuSTAR* team, we used the status expression ‘STATUS= = b0000xxx00xxxx000’ to avoid source photons being spuriously flagged as ‘TEST’ events due to the bright source. The source region was a circle of 60 arcsec radius centroided to the peak brightness. We also extracted a background from a circle of 60 arcsec radius from the area of the same chip with the lowest apparent source contamination. However, this background flux is negligible and source-dominated across the whole bandpass (for the observations analysed here). We group the FPMA data to a minimum signal-to-noise ratio of at least 50, which allows the use of  $\chi^2$  statistics, and group FPMB to the same energy bins to facilitate straightforward comparison of detectors.

To properly account for the loss of exposure due to dead-time and ensure all other instrumental effects are properly accounted for, we produce light curves using the NUPRODUCTS software, which includes the NULCCORR process. To fully account for dead-time, this requires that the light-curve bin size is at least 1 s. When studying higher frequencies than this allows ( $> 0.5$  Hz), we correct for dead-time using the HENDRICS package (Bachetti 2015; Bachetti et al. 2015; Bachetti & Huppenkothen 2018).

To indicate the magnitude of dead-time effects, mean incident count-rates and live fractions for each observation are also given in Table 1.

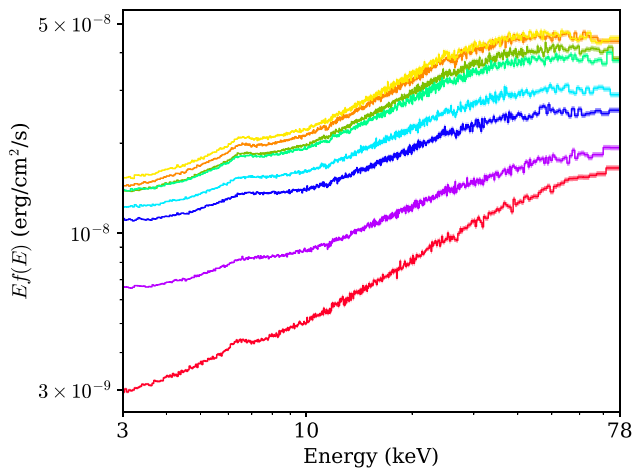


**Figure 3.** Spectra of each *NuSTAR* observation unfolded to a constant model. FPMA and B have been combined for display purposes. The colour of each observation matches that in Fig. 1. The source has almost constant spectral shape during the hard state, softening slowly through the initial outburst, and re-hardening during the second rise.

### 3 RESULTS

#### 3.1 Spectral analysis

##### 3.1.1 Qualitative comparison

The spectrum from each epoch considered here is shown unfolded to a constant model in Fig. 3. Apart from changes in hardness, this shows little evolution in spectral shape throughout the hard state. The spectra soften gradually till the second increase in flux (the last epoch in the hard state, epoch 8, shown in purple), when a slight hardening is seen. To show spectral features more clearly, we also show the hard state spectra as a ratio to the best-fitting power law in Fig. 4. This shows a broad iron  $K\alpha$  emission line peaking around 6.5 keV and a Compton hump at 20–50 keV, indicating the presence of relativistic reflection, as would be expected from an accretion disc extending close to a black hole (e.g. Fabian et al. 2000; Reynolds & Nowak 2003). There is also a clear narrow core to the iron emission. The broad component of the iron line appears remarkably stable throughout the outburst, while the relative strength of the narrow core reduces with time; this behaviour is also seen in observations by *NICER* (Kara et al. 2019). Additionally, the relative high-energy flux increases during the outburst, possibly indicating an increase in coronal temperature. The relative high-energy flux is also significantly greater during increases in broad-band flux (the first and last hard-state spectra) than decreases.

##### 3.1.2 Quantitative modelling

We model the hard X-ray emission as originating from a Comptonizing corona illuminating a disc around a black hole. Owing to the availability of models, we make the standard geometrical approximation of a razor-thin, Keplerian disc. From the change in iron line profile, we deduce that the illumination of the outer disc (forming the narrow core) is changing, while the illumination of the inner disc (forming the broad component) varies less. Therefore, we require an extended, changing corona. We model this simply as two-point sources on the spin axis at different heights above the

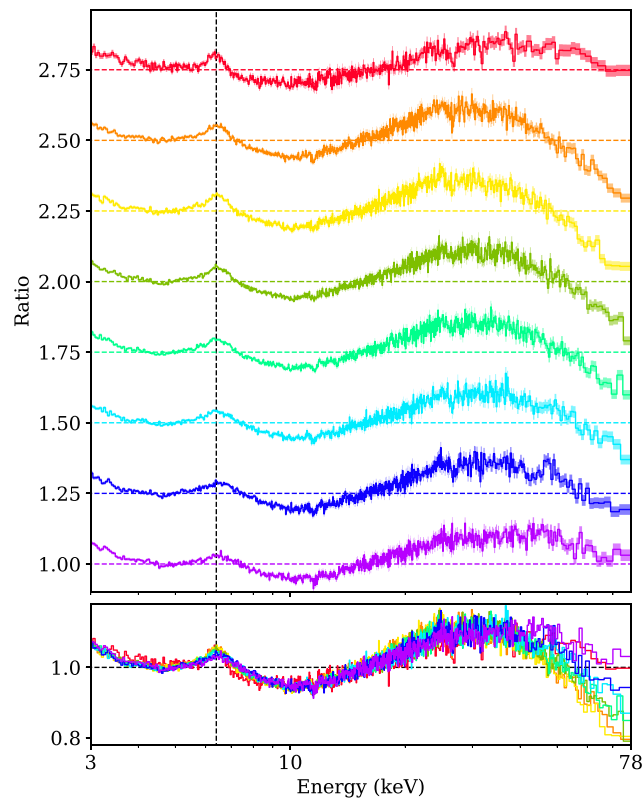


**Figure 4.** Ratio of the mean spectrum of each epoch in the hard state to the best-fitting power law. Time runs from top to bottom in the upper panel; successive epochs are offset by 0.25, as indicated by the dashed lines. All epochs are shown superimposed in the lower panel. The colour of each observation matches that in Fig. 1. The vertical dashed line indicates the rest energy (6.4 keV) of the iron line. The narrow core to the iron line weakens and (apart from the first epoch) the relative high-energy flux increases throughout the outburst. Features at  $\sim 12$  and 28 keV are calibration residuals.

disc (two instances of RELXILLPCP; Dauser et al. 2010; García et al. 2014) with the upper point source inducing the majority of the narrow component of the reflection and the lower point source dominating the broad component. This is unlikely to be the true physical scenario (the true extension is likely continuous, especially once averaged over many dynamical times) but provides a representation with sufficient variable parameters to model the observed changes to the spectra while remaining computationally tractable.

The increase in flux at low energies relative to a simple power law (see Fig. 4) is greater than is present in the reflection in the RELXILLPCP model (which uses XILLVER; García et al. 2013). This may be due to the disc having higher density than is used in (this version of) XILLVER, which has a proton density of  $n = 10^{15} \text{ cm}^{-3}$  as appropriate for typical AGN (García et al. 2016). The higher density causes the reprocessed thermal continuum to move into the X-ray band (García et al. 2016; Tomsick et al. 2018; Jiang et al. 2019a). A detailed analysis of this effect requires data at softer energies than are provided by *NuSTAR* and will be considered in future work (Fabian et al., in preparation); here, we represent the additional soft flux with a DISKBB component.

We fit the data in ISIS (Houck & Denicola 2000) version 1.6.2-41 across the full *NuSTAR* band, 3–78 keV, excluding 11–12 and 23–28 keV due to sharp features that differ between FPMA and B,

**Table 2.** Parameters of fits to MAXI J1820+070 in the hard state. The model is DISKBB+RELXILLPCP(1) + RELXILLPCP(2). Errors represent 90 per cent confidence intervals.

Component	Model	Parameter	Epoch			
			1	2	3	4
Soft flux	DISKBB	Norm <sub>FPMA</sub>	$80^{+40}_{-50}$	$1000^{+800}_{-500}$	$1000^{+700}_{-500}$	$1500^{+900}_{-500}$
		$kT_{\text{FPMA}}/\text{keV}$	$0.8 \pm 0.1$	$0.68^{+0.08}_{-0.05}$	$0.7^{+0.08}_{-0.07}$	$0.64 \pm 0.05$
	DISKBB	Norm <sub>FPMB</sub>	$300^{+100}_{-300}$	$1500^{+2500}_{-900}$	$2000^{+4000}_{-1000}$	$4000^{+3000}_{-2000}$
		$kT_{\text{FPMB}}/\text{keV}$	$0.6^{+0.3}_{-0.2}$	$0.6^{+0.09}_{-0.06}$	$0.58^{+0.09}_{-0.08}$	$0.53^{+0.05}_{-0.06}$
Compton continuum	RELXILLPCP(1/2)	Norm <sub>FPMA</sub>	$0.24 \pm 0.07$	$0.28^{+0.08}_{-0.06}$	$0.32^{+0.07}_{-0.06}$	$0.41^{+0.04}_{-0.08}$
		$C_{\text{FPMB}}/\text{FPMA}$	$1.023 \pm 0.01$	$1.03 \pm 0.002$	$1.031 \pm 0.002$	$1.029 \pm 0.002$
		$\Gamma_{\text{FPMA}}$	$1.508^{+0.005}_{-0.009}$	$1.588^{+0.009}_{-0.01}$	$1.59^{+0.01}_{-0.02}$	$1.6^{+0.011}_{-0.007}$
		$\Gamma_{\text{FPMB}}$	$1.512^{+0.006}_{-0.008}$	$1.589^{+0.009}_{-0.015}$	$1.59 \pm 0.01$	$1.602^{+0.011}_{-0.01}$
		$kT/\text{keV}$	$400^{+0}_{-300}$	$39 \pm 4$	$38^{+4}_{-3}$	$50 \pm 5$
Disc	RELXILLPCP(1/2)	$R_{\text{in}}/r_g$	$4.9^{+2.3}_{-0.5}$	$5.4^{+0.9}_{-0.7}$	$5.9^{+1.2}_{-0.8}$	$5.3^{+1.3}_{-0.5}$
		$\theta/^\circ$	$30^{+4}_{-5}$	$34^{+2}_{-1}$	$32^{+2}_{-3}$	$33^{+3}_{-1}$
		$A_{\text{Fe}}/A_{\text{Fe},\odot}$	$4.0^{+0.9}_{-0.7}$	$5.3^{+2.0}_{-1.0}$	$7^{+1}_{-2}$	$7^{+2}_{-1}$
Lower reflection	RELXILLPCP(1)	$h/r_g$	$3.1^{+1.9}_{-0.9}$	$4.6^{+1.3}_{-0.7}$	$4.4^{+0.9}_{-0.6}$	$3.63^{+0.07}_{-0.05}$
		$\log(\xi/\text{erg cm s}^{-1})$	$3.08^{+0.14}_{-0.05}$	$1.9^{+0.4}_{-0.5}$	$2.3 \pm 0.3$	$2.4^{+0.1}_{-0.2}$
Upper reflection	RELXILLPCP(2)	$h/r_g$	$100^{+0}_{-40}$	$40^{+60}_{-30}$	$40^{+60}_{-20}$	$14^{+9}_{-4}$
		$\log(\xi/\text{erg cm s}^{-1})$	$0^{+2}_{-0}$	$3.9 \pm 0.2$	$3.9 \pm 0.1$	$3.71^{+0.08}_{-0.25}$
	$\chi^2/\text{d.o.f.}$		676.7/624	957.5/895	890.1/864	1267.9/1037
	FPMA to FPMB comparison		1.08	1.07	1.03	1.22
			1.09	1.1	1.0	1.24
Component	Model	Parameter	Epoch			
Soft flux	DISKBB	Norm <sub>FPMA</sub>	$2600^{+2000}_{-700}$	$4000 \pm 2000$	$5000^{+4000}_{-2000}$	$3000^{+2000}_{-1000}$
		$kT_{\text{FPMA}}/\text{keV}$	$0.6^{+0.03}_{-0.05}$	$0.56 \pm 0.05$	$0.53^{+0.04}_{-0.05}$	$0.53^{+0.0}_{-0.02}$
	DISKBB	Norm <sub>FPMB</sub>	$8000^{+13000}_{-4000}$	$6000^{+16000}_{-4000}$	$8000^{+14000}_{-4000}$	$2900^{+500}_{-1700}$
		$kT_{\text{FPMB}}/\text{keV}$	$0.48 \pm 0.05$	$0.48^{+0.09}_{-0.07}$	$0.47^{+0.05}_{-0.06}$	$0.5^{+0.06}_{-0.05}$
Compton continuum	RELXILLPCP(1/2)	Norm <sub>FPMA</sub>	$0.38^{+0.11}_{-0.05}$	$0.4^{+0.3}_{-0.1}$	$0.35347^{+7e-05}_{-0.10446}$	$0.2535^{+0.0002}_{-0.0246}$
		$C_{\text{FPMB}}/\text{FPMA}$	$1.014 \pm 0.002$	$1.016 \pm 0.002$	$1.011 \pm 0.002$	$1.004^{+0.003}_{-0.004}$
		$\Gamma_{\text{FPMA}}$	$1.621^{+0.008}_{-0.006}$	$1.65 \pm 0.01$	$1.658^{+0.009}_{-0.012}$	$1.626^{+0.008}_{-0.006}$
		$\Gamma_{\text{FPMB}}$	$1.623^{+0.008}_{-0.006}$	$1.65^{+0.02}_{-0.01}$	$1.658^{+0.009}_{-0.011}$	$1.63^{+0.004}_{-0.002}$
		$kT/\text{keV}$	$54^{+9}_{-3}$	$80^{+40}_{-20}$	$92^{+76}_{-8}$	$230^{+140}_{-80}$
Disc	RELXILLPCP(1/2)	$R_{\text{in}}/r_g$	$5.8^{+0.7}_{-0.4}$	$4.7^{+1.5}_{-0.8}$	$4.4^{+0.5}_{-0.7}$	$5.6^{+2.6}_{-0.5}$
		$\theta/^\circ$	$31^{+3}_{-2}$	$35^{+4}_{-5}$	$38^{+3}_{-4}$	$36^{+4}_{-5}$
		$A_{\text{Fe}}/A_{\text{Fe},\odot}$	$5.0^{+3.7}_{-0.4}$	$8^{+1}_{-3}$	$10^{+0}_{-4}$	$6.0^{+1.3}_{-1.0}$
Lower reflection	RELXILLPCP(1)	$h/r_g$	$3.6 \pm 0.4$	$3.1^{+0.7}_{-0.5}$	$2.9 \pm 0.6$	$3.7^{+2.0}_{-0.1}$
		$\log(\xi/\text{erg cm s}^{-1})$	$1.7^{+0.8}_{-0.7}$	$2.1^{+0.4}_{-2.1}$	$2.1^{+0.7}_{-2.1}$	$3.48^{+0.14}_{-0.07}$
Upper reflection	RELXILLPCP(2)	$h/r_g$	$16^{+8}_{-5}$	$15^{+12}_{-6}$	$6^{+24}_{-2}$	$100^{+0}_{-70}$
		$\log(\xi/\text{erg cm s}^{-1})$	$3.49^{+0.29}_{-0.04}$	$3.8^{+0.1}_{-0.3}$	$3.9 \pm 0.1$	$0.3^{+1.7}_{-0.3}$
	$\chi^2/\text{d.o.f.}$		1136.9/995	1033.7/909	936.3/849	1032.4/868
	FPMA to FPMB comparison		1.14	1.14	1.1	1.19
			1.14	1.12	1.1	1.13

which we ascribe to instrumental effects (these energies correspond to more variable regions of the empirical correction factor; Madsen et al. 2015, fig. 5). We give parameters in Table 2. The error bars are given and plotted at the 90 per cent level for 1 parameter of interest. Residuals are shown in Fig. 5 and examples of the best-fitting models themselves are shown in Fig. 6. The evolution of the parameters is shown in Fig. 7.

Due to slight calibration differences between FPMA and FPMB, we allow different DISKBB parameters and photon indices ( $\Gamma$ ) between modules. We find that the typical difference in photon index is similar to the uncertainty in the fit, with FPMB always requiring a slightly harder model, though the difference is less than the stated calibration level (Madsen et al. 2015). Similarly, FPMA always has a slightly hotter DISKBB component.

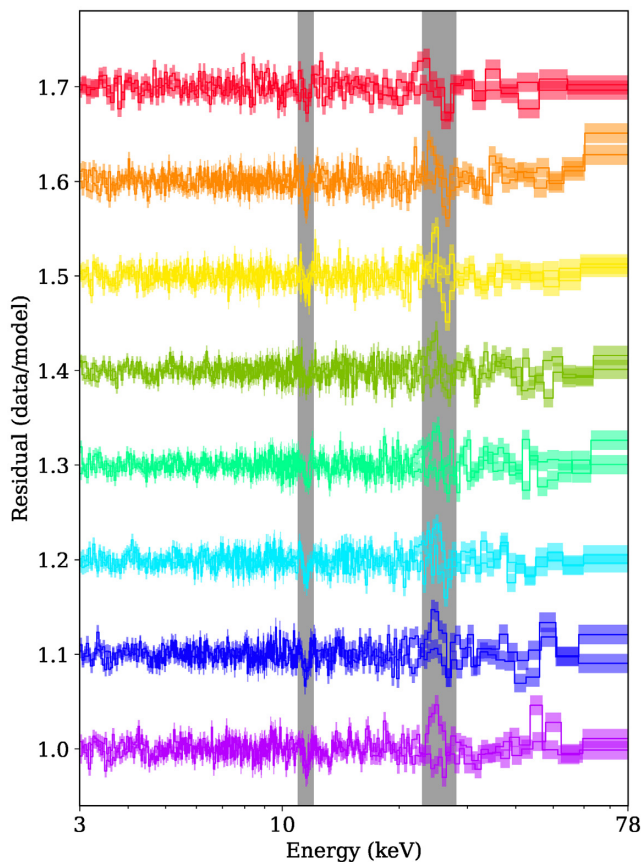


**Figure 5.** Plot of ratio residuals to best-fitting models for each spectrum. Successive spectra are offset by 0.1. The colour of each epoch matches that in Fig. 1. The grey bands denote energy ranges that were ignored for fitting due to instrumental features.

To check that there is statistically significant evidence for the two-point extended corona, we also test a model with a single-point source. This gives a significantly worse fit for each epoch:  $\Delta\chi^2 = 17$  for 3 degrees of freedom in the weakest case, sometimes

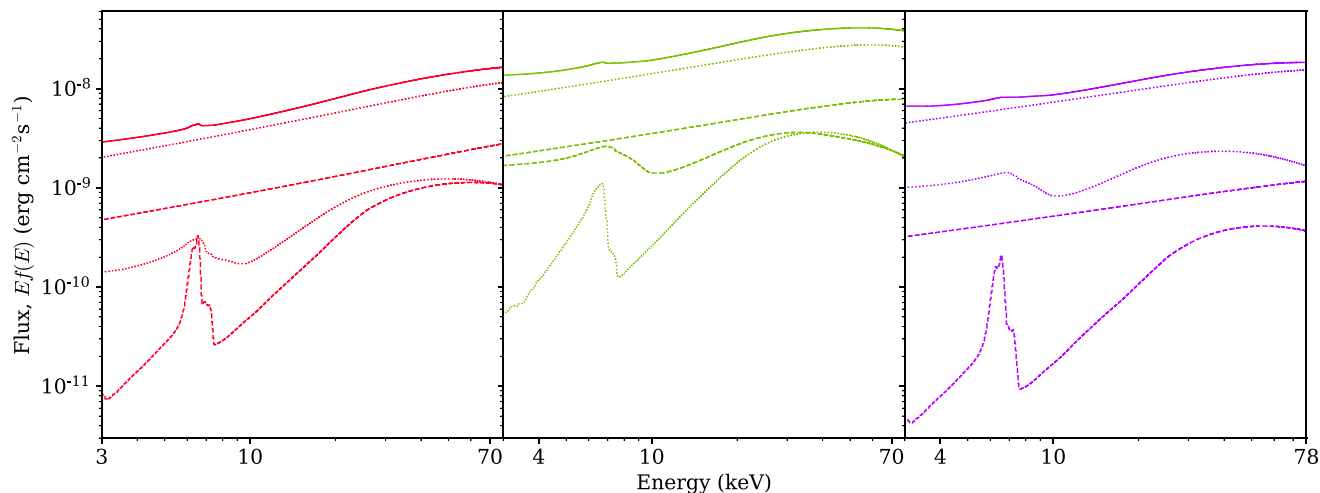


**Figure 6.** Plot of best-fitting models to epochs 1, 4, and 8 (left to right). The colour of each epoch matches that in Fig. 1. The upper line in each epoch is the total model; the contributions from the upper and lower corona are shown dashed and dotted, respectively, each separated into their continuum and reflected components. The relative contribution from the narrow reflection component reduces in successive observations.

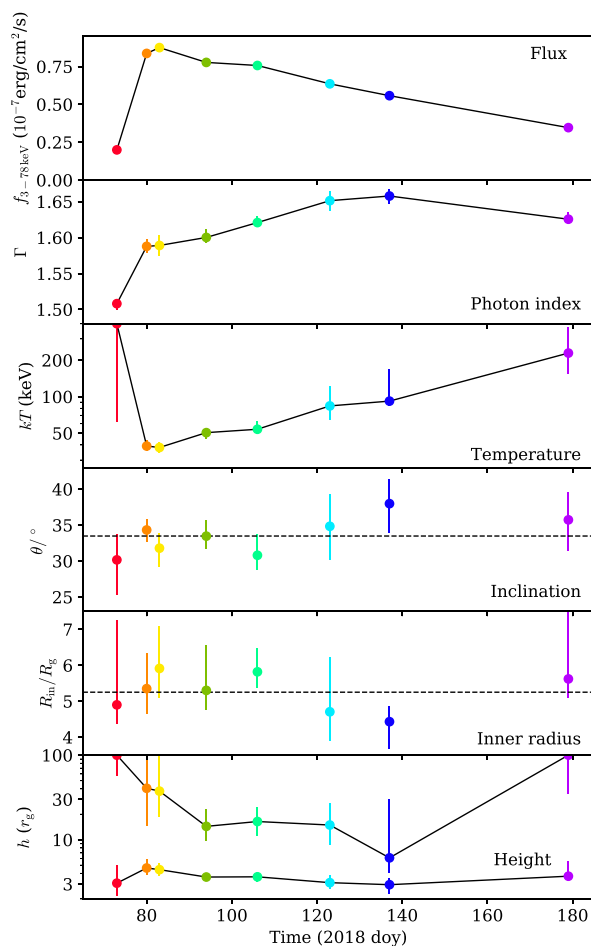


**Figure 7.** Plot of key system parameters against time. The dashed horizontal lines indicate the weighted mean across epochs.

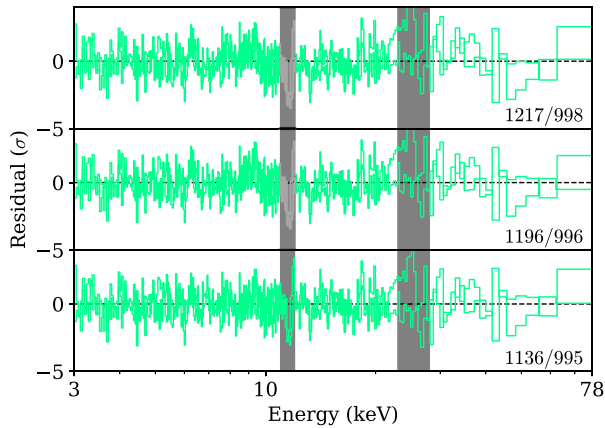


**Figure 8.** Example of residuals for each variant of the model (see text for details). Top: single corona; middle: double corona with tied ionization; bottom: final double corona model. The fit statistic/degrees of freedom is given in the lower right of each panel. All panels show epoch 5 only.

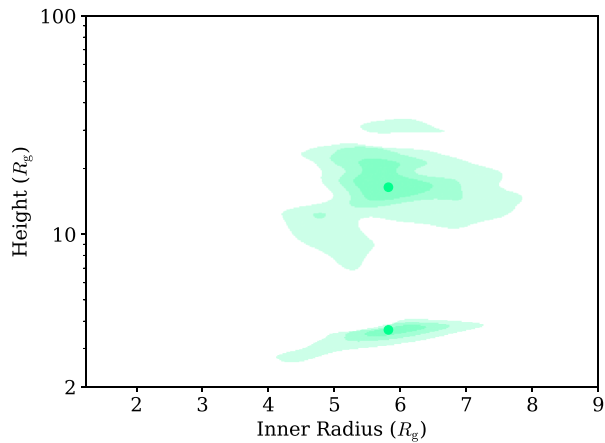


**Figure 9.** Contour plots for the change in fit statistic with coronal height (for each of the two components) and disc inner radius. The colour levels indicate  $1\sigma$ , 90 percent and  $3\sigma$  confidence. For clarity, only epoch 5 is shown as an example.

$\Delta\chi^2 \geq 100$ . An example of the change in residuals for the different models is given in Fig. 8.

We also check that the parameters of the extended corona are reliably constrained, by testing for degeneracies between the height of each coronal component and the disc inner radius. We show the confidence contour plot of  $R_{\text{in}}$  against the height of each coronal component in Fig. 9. This shows that while there is a mild degeneracy between inner radius and lower coronal height, each parameter is independently well constrained.

For self-consistency, we tie black hole parameters and disc parameters that cannot change quickly between the two RELXILLPCP components. We also use the self-consistent reflection fraction (the reflection strength is calculated based on the coronal height; Dauser et al. 2016), so include the continuum contribution from both components. However, as well as the height, we allow the disc ionization to differ between the two components. We find that this difference is statistically necessary, with an average  $\Delta\chi^2$  of 39 per epoch. This can be justified physically in several ways. The different heights in the different components mean that they

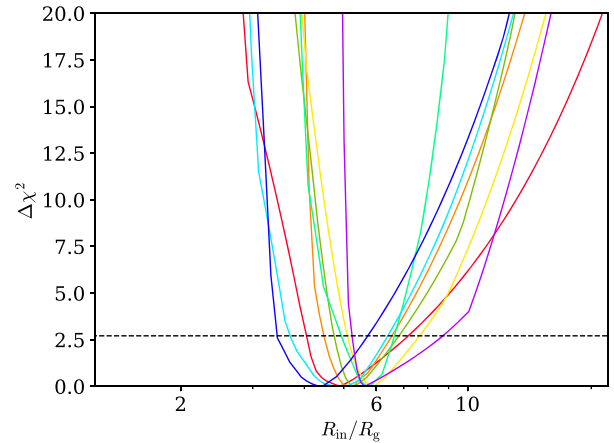


**Figure 10.** Plot of constraint on inner disc radius,  $R_{\text{in}}$ , in terms of change in fit statistic,  $\Delta\chi^2$ , for each epoch. The dashed line indicates the change in  $\chi^2$  corresponding to a 90 per cent confidence interval.

mostly illuminate different regions of the disc (the lower component principally illuminates the inner disc). Alternatively, the variability in the system could be such that the flux from different coronal regions is dominant at different times: the disc ionization could also change with this such that the ionization when the upper corona is dominant differs from that when the lower dominates. The resulting ionization values often differ from the naïve expectation that the lower corona should illuminate a more ionized inner disc. For this to be taken as physical, either some variability allows the disc to be less ionized when emission from the lower corona is dominant or a density gradient allows the more strongly illuminated inner region to have lower ionization. Alternatively, the relative ionization values could be a modelling artefact; in this case, we can check the reliability of other parameters by tying both ionization values together. Testing this on epoch 4 data (which has the strongest signal) retrieves parameters that are similar to (and in particular the inner radius is consistent at the 90 per cent level with) the values from the fits in Table 2.

Owing to the strong degeneracy between black hole spin and disc truncation, we fit for inner radius,  $R_{\text{in}}$ , in a maximally spinning (dimensionless spin parameter  $a = 0.998$ ) space–time. The resulting values show little spread around their weighted mean,  $R_{\text{in}} \sim 5.3 r_g$  ( $r_g = GM_{\text{BH}}/c^2$ ), see Fig. 10. If this radius is  $R_{\text{ISCO}}$ , it implies a low-spin black hole. A full estimate of the black hole spin, including low-energy data from *NICER*, will be presented in a forthcoming paper (Fabian et al., in preparation).

The iron abundance of the disc is found to be significantly higher than solar ( $A_{\text{Fe}} \sim 5A_{\text{Fe},\odot}$ ). This is not necessarily unexpected, since stars vary in metallicity, but the value found is likely to be an overestimate, particularly given the ubiquity of apparent supersolar iron abundances (García et al. 2018). The overestimate could be due to a higher density disc (as predicted for stellar mass black holes; Svensson & Zdziarski 1994; García et al. 2016), which would show stronger iron lines at a given metallicity (García et al. 2016; Tomsick et al. 2018; Jiang et al. 2019b). The difference in density should not have a strong effect on other parameters of the system. Additionally, high metallicity could occur if the supernova that formed the black hole polluted the surface of the companion with metal-rich material, which is now being accreted.

Many of these fits are formally poor, in the sense of having low null hypothesis probabilities. However, the statistical errors in the

spectrum are comparable to the calibration precision of *NuSTAR* due to the extremely high signal in the data sets used here, so calibration differences between the detectors may lead to inflated  $\chi^2$  values. To give a guide to how significant this effect is, we also show the value:

$$\frac{((D_A - M_A) - (D_B - M_B))^2}{(E_A^2 + E_B^2) \times \text{d.o.f.}},$$

where  $D_i$ ,  $M_i$ ,  $E_i$  are the data, model, and error values, respectively, for detector  $i$  and d.o.f. is the number of degrees of freedom, i.e. the number of bins minus the six variables in our model, which can differ between detectors (4 from two instances of DISKBB; the normalization difference; and the difference in  $\Gamma$ ). This is essentially a reduced  $\chi^2$  value testing that FPMA matches FPMB. All values are similar to the reduced  $\chi^2$  found for the respective source model. Since the model cannot simultaneously match both detectors better than the detectors match each other, this justifies the fit quality of the source models.

Another way of determining the effects of calibration uncertainties is to add a systematic error to the measurement uncertainties; here, a systematic error of below 0.5 per cent brings the reduced  $\chi^2$  to unity; the effects on parameters of interest are minor. Since the effects of systematic error are binning dependent and the level chosen is somewhat arbitrary, we consider the parameters derived without addition of systematic error for the rest of this work.

Various parameters (e.g. coronal temperature) change significantly between epochs. How these changes are related, to each other and to properties of the rapid variability, is considered further in Section 4.

### 3.2 Variability analysis: power spectra

The time-scales on which a source varies may be quantified with the power spectral distribution (PSD; e.g. Priestley 1981):

$$P(f) = |A(f)|^2$$

where  $A(f)$  is the Fourier transform of the flux at frequency  $f$ .

Initially, we produce periodograms from the full calibrated *NuSTAR* band (3–78 keV), using light-curve segments of 1024 s with  $0.0625 \text{ s} = 1/16 \text{ s}$  bins. We then produce PSDs from the average of all periodograms in an epoch, binning frequencies if necessary to ensure that each PSD data point is produced from at least 20 periodogram values (so that the error on the PSD value is approximately Gaussian). We estimate the size of the error of each PSD point from the variance of the periodogram values which produce it.

These PSDs are shown for each epoch in Fig. 11. The low-frequency cut-off in power increases in break frequency as the outburst progresses. Additionally, a QPO is present close to the break frequency in each observation (although its detection is very marginal in the first); a further peak is present close to double the primary QPO frequency. These QPO frequencies also (with the exception of the final observation) increase with time.

We also test for changes in variability properties with energy by splitting each light curve into five energy bands (3–5, 5–6, 6–9, 9–13, and 13–78 keV) with approximately equal counts. This shows a similar PSD shape in each band and only a slight change in variability amplitude. Therefore, we consider only the full band PSDs here (a detailed analysis of the changes with energy will be presented as part of a future work).

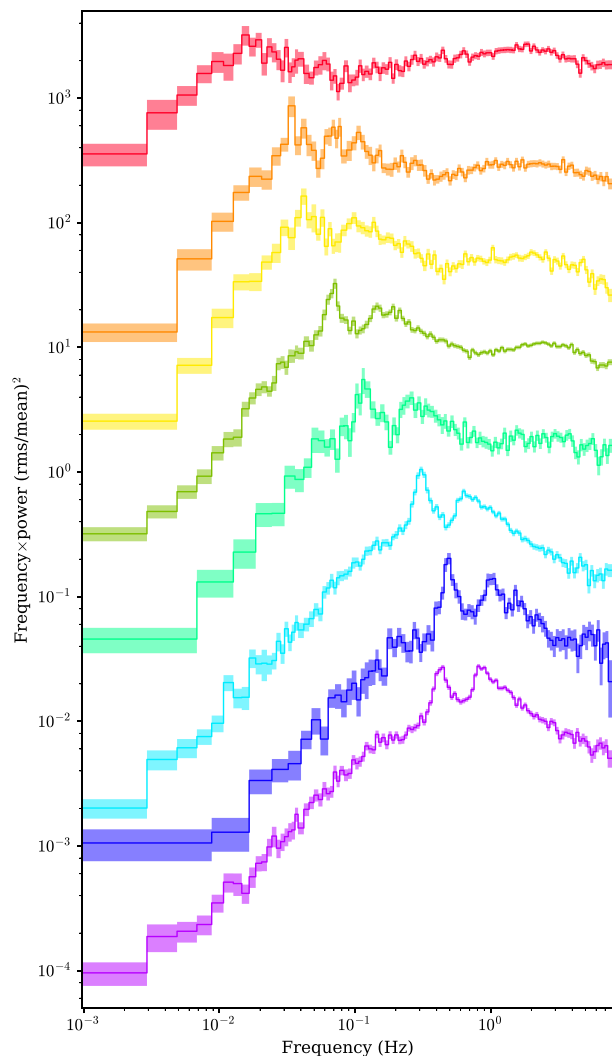


**Figure 11.** PSDs of *NuSTAR* data, with the RMS normalization. Successive PSDs are offset by a factor of 5. Poisson noise has been subtracted based on the best-fitting values and each PSD has been rebinned to a geometric progression of at least 1.05 for clarity. Frequencies of features in the PSD (QPO and low-frequency break) increase over the first section of the outburst. During the latter stages of the outburst, the variability decreases.

#### 3.2.1 Fitting

Power spectra of accreting black holes can typically be fit with the sum of several Lorentzians (Olive et al. 1998; Belloni, Psaltis & van der Klis 2002). We fit such a model, typically using five Lorentzians (apart from epochs 1 where only 3 are necessary, 4 where 6 are necessary, and 7 where 4 are necessary), and including an additional constant (independent of frequency) component for the Poisson noise. We fit the two FPMs as separate data sets with the same source model but independent Poisson noise components.

We then use Markov Chain Monte Carlo methods to fit each of the PSDs, utilizing the XSPEC\_EMCEE implementation.<sup>1</sup> We use 150 walkers for 5000 steps after a burn in period of 1000 steps. For

<sup>1</sup>Written by Jeremy Sanders, based on the EMCEE package (Foreman-Mackey et al. 2013).

**Table 3.** Parameters of QPO fundamental for each epoch analysed. Epoch 1 does not have a clear detection of the QPO, so is not included.

Epoch	$\nu_{\text{peak}}$	$Q$
2	$0.036^{+0.002}_{-0.002}$	$3.1^{+1.3}_{-0.8}$
3	$0.041^{+0.003}_{-0.002}$	$2.5^{+1.6}_{-0.5}$
4	$0.068^{+0.001}_{-0.001}$	$7.7^{+2.2}_{-1.5}$
5	$0.117^{+0.006}_{-0.006}$	$6.5^{+7.6}_{-3.0}$
6	$0.308^{+0.002}_{-0.002}$	$8.5^{+0.8}_{-0.7}$
7	$0.489^{+0.007}_{-0.006}$	$10.5^{+2.9}_{-2.3}$
8	$0.428^{+0.036}_{-0.004}$	$7.9^{+1.1}_{-4.9}$

each parameter, we apply a simple uniform prior across a range determined by eye to encompass all reasonable values.

We then extract characteristic time-scales to compare with spectral properties. We extract the QPO peak frequency ( $\nu_{\text{peak}} = \sqrt{\nu_0^2 + \sigma^2}$ ) by finding the narrow Lorentzian with the highest normalization close to the visible QPO peak frequency (where the allowed range is determined by eye to exclude adjacent peaks). We define a Lorentzian as narrow based on the standard threshold,  $Q > 2$ , where  $Q = \sigma/2\nu_0$  is the quality factor. Epoch 1 does not have a clear QPO, so we do not extract a QPO frequency for it. We show the derived parameter values in Table 3. We note that the low-frequency break follows the change in QPO frequency; due to the similar changes in each characteristic frequency and the complication in reliably extracting the low-frequency break from the multiple Lorentzian model, we do not consider the low-frequency break quantitatively.

#### 4 COMPARISON OF PARAMETER EVOLUTION AND DISCUSSION

We have described the evolution of the hard X-ray emission from the initial hard state of MAXI J1820+070. This is a powerful probe of the inner accretion system and our analysis shows a reflecting inner disc extending close to the ISCO of the central black hole throughout the hard state of the outburst. This is in stark contrast to the large change in variability time-scale, which increases by a factor of around 30. We also find changes in the coronal temperature and extent.

We compare how key parameters evolve with respect to each other in Fig. 12. While many pairs of parameters appear uncorrelated, there are correlations between the coronal temperature and each of QPO frequency and flux. We discuss possible reasons for the changes (or lack thereof) of system properties and their correlations in the following subsections.

##### 4.1 Disc inner radius

One important issue that is not yet fully resolved is when during an outburst the disc is truncated. Here, we have shown several observations in the hard state without strong disc truncation. To be consistent with observations of truncated discs at low accretion rate (Tomsick et al. 2009), this implies that the disc fills (the inner radius moves inwards) during the initial rise: most of the observations used here are at or after the peak of the outburst. This would imply that discs can reach close to the ISCO regardless of hard/soft state, in this case showing bright hard state emission with a reflecting disc at or close to the ISCO.

##### 4.2 QPO frequency

QPOs are often found in the power spectra of X-ray binaries, though their origin is not yet fully understood. Such QPOs are a rapidly oscillating change in the flux of the source. They are observed to occur principally in the coronal power law emission (Rodríguez et al. 2002; Casella et al. 2004) but most explanations invoke some link to the disc, as the disc possesses more accessible characteristic time-scales, particularly those associated with the inner edge.

Various models associate the inner disc radius with the characteristic scale, which produces QPOs. We plot our measurements of QPO frequency and inner radius along with some models in Fig. 13 (similar to Fürst et al. 2016). First, relativistic effects introduce various precession frequencies. Of these, Lense–Thirring (nodal) precession is most likely to lie in the frequency range of LFQPOs (Stella & Vietri 1998; Stella et al. 1999). Following Ingram et al. (2009), we plot the frequencies of a single particle and a hot flow extending to  $R_{\text{ISCO}}$  (we do not show a hot flow with the inner radius set by bending waves as this radius is always larger than our measurements). For illustration, we take a black hole mass  $M_{\text{BH}} = 100 M_{\odot}$  (a high mass is required to have low enough frequencies); a radial surface density profile ( $\Sigma \propto r^{-\zeta}$ ) having  $\zeta = 0$  to match simulations (Fragile et al. 2007); and choose  $a = 0.3$  to give similar frequencies to those observed while not having the measured  $R_{\text{in}} < R_{\text{ISCO}}$ . Another possibility is an oscillation mode of the disc, such as the global normal disc oscillation discussed in Titarchuk & Osherovich (2000): an oscillation of the whole disc in the direction normal to the disc plane. We also plot this in Fig. 13, again taking  $M_{\text{BH}} = 100 M_{\odot}$  and choosing the outer disc radius,  $r_{\text{out}} = 10^4 r_g$  to give reasonable frequencies. All of these models require a much greater change in inner radius than is measured to explain the range of QPO frequencies. Therefore, either some other process governs the frequency of QPOs or the inner radius of the reflecting material does not match the edge of the oscillating material.

Our results show a change in QPO frequency without a significant change in disc inner radius (see also Fürst et al. 2016; Xu et al. 2017), which is a challenge for models that rely on geometric (orbital or precession) time-scales related to the inner edge of the disc. Since QPOs appear to have different observed properties depending on inclination (van den Eijnden et al. 2017), some geometric effects are likely; these could still occur but be linked to the frequency differently, such as jet precession, or indirectly, such as a coronal oscillation, which is directed parallel to the plane of the disc.

There are other possible models for QPO production: it has also been suggested that feedback between coronal heating of the disc and increased seed photon rates could have resonant frequencies that manifest as QPOs.

Alternatively, the QPO could be generated directly by oscillations in the corona (e.g. Zanotti et al. 2005; Cabanac et al. 2010), such as a resonant mode of the constituent plasma. A simple prescription to describe this could be a sound wave passing across the corona. The frequency then scales as

$$\nu = A \frac{c_s}{2d} \simeq A \frac{T_9^{1/2}}{d_2} \text{ Hz}$$

where  $c_s$  is the sound speed,  $T = 10^9 T_9$  K is the temperature,  $d = 100 d_2 r_g$  is the distance across the corona, and  $A$  is a factor of order unity. This would fit with the change in coronal extent and temperature implied by the spectral fitting – in the smaller, hotter corona, oscillations would have a higher frequency. More quantitatively, during the outburst the coronal height reduces by

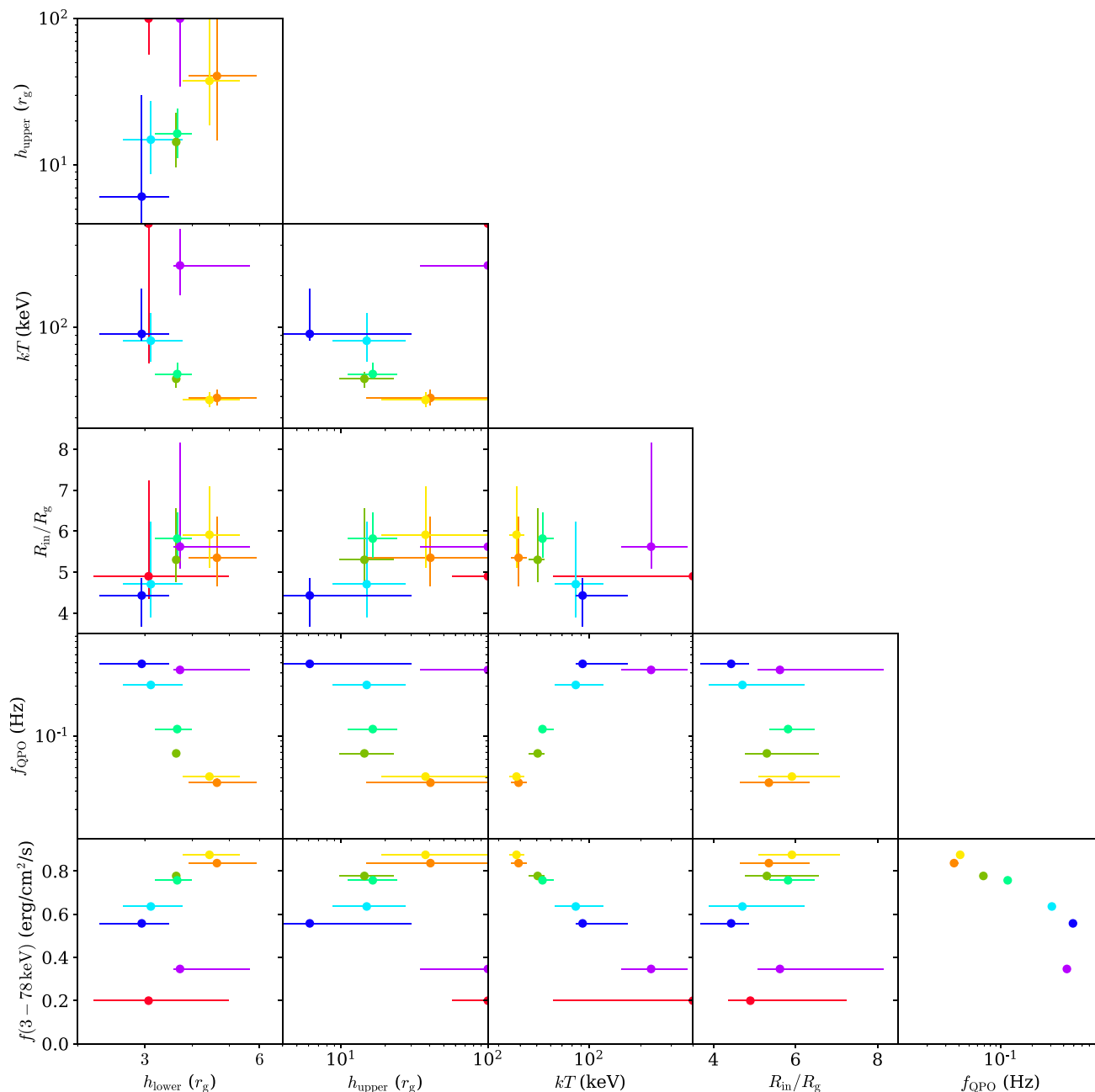


**Figure 12.** Plot comparing evolution of different parameters. The colour of each epoch matches previous figures. Correlations are present between various parameters – see text for details.

around a factor of 10 and the temperature increases by a factor of at least 4. This would increase the associated frequency by a factor of  $\sim 20$ , similar to the observed increase in QPO frequency. The average value of  $A$  for  $\nu$  to match  $\nu_{\text{QPO}}$  is then  $\sim 1/30$  (taking  $M_{\text{BH}} = 10 M_{\odot}$ ). This factor could include contributions from the turnaround time at each end of the corona or from other physical processes. magnetohydrodynamic calculations (Edwin & Roberts 1983) show that magnetic fields affect the frequency of various modes of oscillation. Detailed calculations of expected values of  $A$  are beyond the scope of this work.

Remillard & McClintock (2006; fig. 10) show that QPO frequency correlates with disc flux in hard/steep power-law-intermediate states. The observations presented here have a weaker

disc component, which is not unambiguously detected but may be clearer at soft energies, so this could be investigated, for example, with *NICER*.

While the QPO is most dominant at high energies, it is also strongly detected in the 3–10 keV band, which is also covered by *NICER*. Owing to the more frequent coverage of MAXI J1820+070 by *NICER*, a more detailed analysis of the QPO progression can be made with these data.

#### 4.3 Coronal temperature

The corona also shows changes in its mean properties: the temperature anticorrelates with flux. This has been observed in other

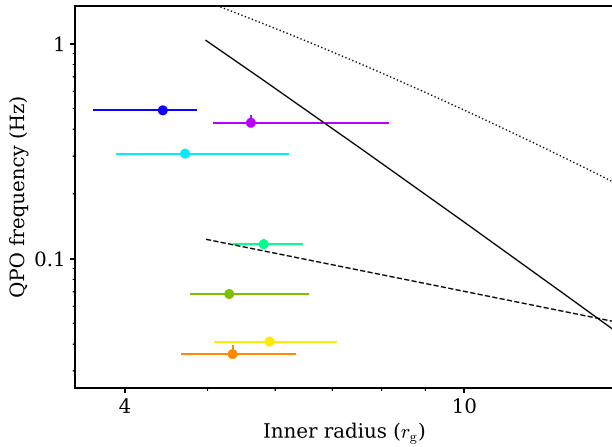


**Figure 13.** Comparison of relation between inner radius and QPO frequency with various models. Solid: Lense-Thirring frequency of particle at  $R_{\text{in}}$ . Dotted: solid-body precession of hot flow extending from  $R_{\text{ISCO}}$  to  $R_{\text{in}}$ . Dashed: Global Normal Disk Oscillation (see text for details of each model). To reproduce the observed range of QPO frequencies, all these models require a significantly greater change in inner disc radius than is measured.

individual XRBs (Joinet, Kalemci & Senziani 2008; Motta, Belloni & Homan 2009) and AGN (Lubiński et al. 2010). This could happen because pair production from photon collisions is regulating the temperature (Svensson 1984; Zdziarski 1985; Fabian et al. 2015): at higher fluxes, there are more photons, which allows sufficient pairs to be produced at lower temperatures. The coronal temperatures observed here are allowed by the pair thermostat, being below the pair-production limit that is observed to limit accreting sources as a population (Fabian et al. 2015). The lower temperatures than the pair limit can be explained by a deviation from a pure thermal distribution, which is expected as the cooling time-scale is less than the collision time-scale (Fabian et al. 2017). The presence of a non-thermal tail to the particle distribution reduces the critical temperature (Fabian et al. 2017). These considerations do not take substructure in the corona into account; this remains a potential caveat when estimating the coronal compactness from its total luminosity and size.

We consider this correlation in more detail by comparing the corona’s radiative compactness with its electron temperature. We take electron temperatures from our fits and calculate the coronal

compactness following the methodology of Fabian et al. (2015). We take the luminosity from the total direct flux of our best-fitting models at a distance of 3.5 kpc. Calculation of the compactness also requires a radius; the coronal prescription used here (including coronal contributions from two points) does not readily convert to an equivalent spherical size so we try several prescriptions. First, we consider a fiducial  $10r_g$  size for all observations. We also consider the effect of a shrinking radius, as could be implied by the reduction in illumination of the outer disc with time. We reduce the radius linearly by epoch from  $10r_g$  to  $5r_g$ , guided by the fractional change in the lag amplitudes from Kara et al. (2019) (since the lags are driven by the location of the majority of flux). We plot these measurements in Fig. 14. The constant coronal size prescription gives a smooth trend but does not align with an obvious physical locus (such as constant non-thermal fraction,  $\ell_{\text{nth}}/\ell_{\text{h}}$ ). The shrinking corona has an approximately constant compactness for all epochs after the peak (i.e. not the first epoch). With these size prescriptions, the non-thermal fraction is higher at high flux. We could instead assume consistent physical conditions within the corona, manifesting as a constant non-thermal fraction, and use this to infer a trend in effective coronal radius: increasing  $r_{\text{Corona}}$  from 5 to  $15r_g$  gives a roughly constant non-thermal fraction of around 20 per cent. This would imply an anticorrelation between the vertical coronal extent and the effective coronal radius, so that the corona had changed shape from prolate or cylindrical to oblate. If this is the case and the QPO frequency is associated with coronal size, then the observed trend in QPO frequency would imply that the vertical, rather than horizontal, extent is the relevant dimension. We stress that these relations depend strongly on the assumed prescription for any change in coronal radius, so must be treated with caution.

This paper covers only a small part of the data available on this outburst: further work on this and similar outbursts with the new generation of facilities now available will surely help to resolve these outstanding questions.

## 5 CONCLUSIONS

We have described the evolution of X-ray spectral and timing properties of the recent outburst of MAXI J1820+070 during the hard state. In particular,

- (i) spectral features change subtly: the broad component of the iron line remains almost constant while the narrow core reduces with time;

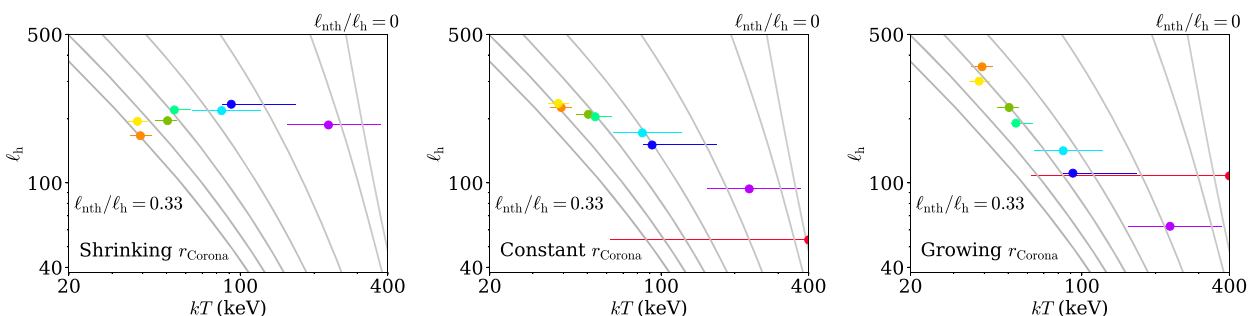


**Figure 14.** Coronal compactness compared with coronal temperature at each epoch. Theoretical curves of constant non-thermal fraction (the grey lines) are taken from Fabian et al. (2017); these have, from right to left,  $\ell_{\text{nth}}/\ell_{\text{h}} = 0, 0.01, 0.09, 0.17, 0.23, 0.29, 0.33$ . Data from each epoch have the same colours as other figures. Errors in  $\ell_{\text{h}}$  are dominated by the choice of coronal radius so the error bars are not shown; instead, different choices are given in the different panels. The left-hand panel uses a coronal radius decreasing linearly from  $10r_g$  to  $5r_g$ ; the centre panel uses a constant coronal radius of  $10r_g$ ; and the right-hand panel uses a coronal radius, which increases from  $5r_g$  to  $15r_g$  (see text).

(ii) reflection modelling implies a small inner radius in all observations, consistent with the ISCO of a low to moderate spin black hole ( $\sim 5.3r_g$ );

(iii) the change in the iron line shape can be explained by coronal emission being more concentrated close to the black hole in later observations;

(iv) the coronal temperature is higher at lower flux. It can be explained by pair-production if the effective radius of the corona grows with time and the non-thermal electron fraction is  $\sim 20$  per cent;

(v) characteristic frequencies of the variability, QPO frequency, and low-frequency cut-off, increase by a factor of  $\sim 30$  during this outburst state;

(vi) and the change in QPO frequency with stable  $R_{in}$  is hard to reconcile with hot inner disc precession models for QPOs. It is probably related to the temporal development of the corona.

## ACKNOWLEDGEMENTS

We thank Fiona Harrison for approval of these DDT observations and Karl Forster for their prompt scheduling. DJKB acknowledges financial support from the Science and Technology Facilities Council (STFC). ACF acknowledges support from the ERC Advanced Grant FEEDBACK 340442. AWS is supported by an NSERC Discovery Grant and a Discovery Accelerator Supplement. This work has used data from the *NuSTAR* mission, a project led by the California Institute of Technology, managed by the Jet Propulsion Laboratory, and funded by the National Aeronautics and Space Administration. This research has used the NuSTARDAS jointly developed by the ASI Science Data Center (ASDC, Italy) and the California Institute of Technology (USA).

## REFERENCES

- Bachetti M., 2015, *Astrophysics Source Code Library*, record ascl:1502.021
- Bachetti M., Huppenkothen D., 2018, *ApJ*, 853, L21
- Bachetti M. et al., 2015, *ApJ*, 800, 109
- Belloni T., Psaltis D., van der Klis M., 2002, *ApJ*, 572, 392
- Buisson D., Fabian A., Alston W., Walton D., Kara E., García J., Homan J., Tomsick J., 2018, *Astron. Telegram*, 11578, 1
- Cabanac C., Henri G., Petrucci P.-O., Malzac J., Ferreira J., Belloni T. M., 2010, *MNRAS*, 404, 738
- Casella P., Belloni T., Homan J., Stella L., 2004, *A&A*, 426, 587
- Dauser T., Wilms J., Reynolds C. S., Brenneman L. W., 2010, *MNRAS*, 409, 1534
- Dauser T., García J., Walton D. J., Eikmann W., Kallman T., McClintock J., Wilms J., 2016, *A&A*, 590, A76
- Denisenko D., 2018, *Astron. Telegram*, 11400, 1
- Done C., Gierliński M., Kubota A., 2007, *A&AR*, 15, 1
- Edwin P. M., Roberts B., 1983, *Sol. Phys.*, 88, 179
- Esin A. A., McClintock J. E., Narayan R., 1997, *ApJ*, 489, 865
- Fabian A. C., Iwasawa K., Reynolds C. S., Young A. J., 2000, *PASP*, 112, 1145
- Fabian A. C. et al., 2012, *MNRAS*, 424, 217
- Fabian A. C., Lohfink A., Kara E., Parker M. L., Vasudevan R., Reynolds C. S., 2015, *MNRAS*, 451, 4375
- Fabian A. C., Lohfink A., Belmont R., Malzac J., Coppi P., 2017, *MNRAS*, 467, 2566
- Fiori M. et al., 2018, *Astron. Telegram*, 11824, 1
- Foreman-Mackey D., Hogg D. W., Lang D., Goodman J., 2013, *PASP*, 125, 306
- Fragile P. C., Blaes O. M., Anninos P., Salmonson J. D., 2007, *ApJ*, 668, 417
- Fürst F. et al., 2016, *ApJ*, 828, 34
- Gandhi P., Rao A., Johnson M. A. C., Paice J. A., Maccarone T. J., 2019, *MNRAS*, 485, 2642
- García J., Dauser T., Reynolds C. S., Kallman T. R., McClintock J. E., Wilms J., Eikmann W., 2013, *ApJ*, 768, 146
- García J. et al., 2014, *ApJ*, 782, 76
- García J. A., Fabian A. C., Kallman T. R., Dauser T., Parker M. L., McClintock J. E., Steiner J. F., Wilms J., 2016, *MNRAS*, 462, 751
- García J. A., Kallman T. R., Bautista M., Mendoza C., Deprince J., Palmeri P., Quinet P., 2018, in Mendoza C., Turck-Chièze S., Colgan J., eds, *ASP Conf. Ser. Vol. 515, Workshop on Astrophysical Opacities*. Astron. Soc. Pac., San Francisco, p. 282
- Gehrels N. et al., 2004, *ApJ*, 611, 1005
- Gendreau K. C. et al., 2016, in den Herder A. J.-W., Takahashi T., Bautz M., eds, *Proc. SPIE Conf. Ser. Vol. 9905, Space Telescopes and Instrumentation 2016: Ultraviolet to Gamma Ray*. SPIE, Bellingham, p. 99051H
- Gierliński M., Done C., 2004, *MNRAS*, 347, 885
- Gilfanov M., 2010, in Belloni T., ed., *Lecture Notes in Physics*, Vol. 794, *The Jet Paradigm*. Springer-Verlag, Berlin, p. 17
- Harrison F. A. et al., 2013, *ApJ*, 770, 103
- Homan J., Wijnands R., van der Klis M., Belloni T., van Paradijs J., Klein-Wolt M., Fender R., Méndez M., 2001, *ApJS*, 132, 377
- Homan J. et al., 2018, *Astron. Telegram*, 11576, 1
- Houck J. C., Denicola L. A., 2000, in Manset N., Veillet C., Crabtree D., eds, *ASP Conf. Ser. Vol. 216, Astronomical Data Analysis Software and Systems IX*. Astron. Soc. Pac., San Francisco, p. 591
- Ingram A., Done C., 2011, *MNRAS*, 415, 2323
- Ingram A., Done C., Fragile P. C., 2009, *MNRAS*, 397, L101
- Jiang J. et al., 2019a, *MNRAS*, 489, 3436
- Jiang J., Fabian A. C., Wang J., Walton D. J., García J. A., Parker M. L., Steiner J. F., Tomsick J. A., 2019b, *MNRAS*, 484, 1972
- Joinet A., Kalemci E., Senziani F., 2008, *ApJ*, 679, 655
- Kara E. et al., 2019, *Nature*, 565, 198
- Kawamuro T. et al., 2018, *Astron. Telegram*, 11399, 1
- Krimm H. A. et al., 2013, *ApJS*, 209, 14
- Lubiński P., Zdziarski A. A., Walter R., Paltani S., Beckmann V., Soldi S., Ferrigno C., Courvoisier T. J.-L., 2010, *MNRAS*, 408, 1851
- Madsen K. K. et al., 2015, *ApJS*, 220, 8
- Markoff S., Nowak M. A., Wilms J., 2005, *ApJ*, 635, 1203
- Matsuoka M. et al., 2009, *PASJ*, 61, 999
- Mereminskiy I. A., Grebenev S. A., Molokov S. V., Zaznobin I. A., Khorunzhev G. A., Burenin R. A., Eiselevich M. V., 2018, *Astron. Telegram*, 11488, 1
- Motta S., Belloni T., Homan J., 2009, *MNRAS*, 400, 1603
- Novikov I. D., Thorne K. S., 1973, in Dewitt C., Dewitt B. S., eds, *Black Holes (Les Astres Occlus)*. Gordon and Breach, New York, p. 343
- Olive J. F., Barret D., Boirin L., Grindlay J. E., Swank J. H., Smale A. P., 1998, *A&A*, 333, 942
- Parker M. L. et al., 2015, *ApJ*, 808, 9
- Park S. Q. et al., 2004, *ApJ*, 610, 378
- Priestley M., 1981, *Spectral Analysis and Time Series*. Academic Press, London
- Reis R. C., Fabian A. C., Miller J. M., 2010, *MNRAS*, 402, 836
- Reis R. C., Miller J. M., Reynolds M. T., Fabian A. C., Walton D. J., Cackett E., Steiner J. F., 2013, *ApJ*, 763, 48
- Remillard R. A., McClintock J. E., 2006, *ARA&A*, 44, 49
- Remillard R. A., Muno M. P., McClintock J. E., Orosz J. A., 2002, *ApJ*, 580, 1030
- Reynolds C. S., Nowak M. A., 2003, *Phys. Rep.*, 377, 389
- Rodríguez J., Durouchoux P., Mirabel I. F., Ueda Y., Tagger M., Yamaoka K., 2002, *A&A*, 386, 271
- Roques J.-P., Jourdain E., 2019, *ApJ*, 870, 92
- Shakura N. I., Sunyaev R. A., 1973, *A&A*, 24, 337
- Shappee B. J. et al., 2014, *ApJ*, 788, 48
- Shidatsu M. et al., 2018, *ApJ*, 868, 54
- Steiner J. F., McClintock J. E., Remillard R. A., Gou L., Yamada S., Narayan R., 2010, *ApJ*, 718, L117

- Stella L., Vietri M., 1998, *ApJ*, 492, L59  
Stella L., Vietri M., Morsink S. M., 1999, *ApJL*, 524, L63  
Sunyaev R. A., Truemper J., 1979, *Nature*, 279, 506  
Svensson R., 1984, *MNRAS*, 209, 175  
Svensson R., Zdziarski A. A., 1994, *ApJ*, 436, 599  
Thorne K. S., Price R. H., 1975, *ApJ*, 195, L101  
Titarchuk L., Osherovich V., 2000, *ApJ*, 542, L111  
Tomsick J. A., Yamaoka K., Corbel S., Kaaret P., Kalemci E., Migliari S., 2009, *ApJ*, 707, L87  
Tomsick J. A. et al., 2018, *ApJ*, 855, 3  
Tucker M. A. et al., 2018, *ApJ*, 867, L9  
van den Eijnden J., Ingram A., Uttley P., Motta S. E., Belloni T. M., Gardenier D. W., 2017, *MNRAS*, 464, 2643  
van der Klis M., 2006, *Rapid X-ray Variability*. Cambridge Univ. Press, Cambridge, p. 39  
Wijnands R., Homan J., van der Klis M., 1999, *ApJ*, 526, L33  
Winkler C. et al., 2003, *A&A*, 411, L1  
Xu Y. et al., 2017, *ApJ*, 851, 103  
Yu W., Zhang J., Yan Z., Wang X., Bai J., 2018a, *Astron. Telegram*, 11510  
Yu W., Lin J., Mao D., Zhang J., Yan Z., Bai J., 2018b, *Astron. Telegram*, 11591  
Zampieri L., Fiori M., Burtovoi A., Naletto G., Barbieri C., Ochner P., Umbriaco G., Barbieri M., 2018, *Astron. Telegram*, 11723, 1  
Zanotti O., Font J. A., Rezzolla L., Montero P. J., 2005, *MNRAS*, 356, 1371  
Zdziarski A. A., 1985, *ApJ*, 289, 514

This paper has been typeset from a  $\text{\TeX/L\TeX}$  file prepared by the author.